Chinese Chemical Letters 35 (2024) 109552

Contents lists available at ScienceDirect

Chinese Chemical Letters

journal homepage: www.elsevier.com/locate/cclet

In-situ growth of N-doped graphene-like carbon/MOF nanocomposites for high-performance supercapacitor

Wenhao Feng[a], Chunli Liu[b], Zheng Liu[a], Huan Pang[a,*]

[a] School of Chemistry and Chemical Engineering, Yangzhou University, Yangzhou 225002, China
[b] School of Chemistry, Xi'an Jiaotong University, Xi'an 710049, China

ARTICLE INFO

Article history:
Received 29 November 2023
Revised 4 January 2024
Accepted 19 January 2024
Available online 23 January 2024

Keywords:
Supercapacitor
Synergistic effect
MOF
Graphene-like materials
Nanocomposites

ABSTRACT

Graphene-like materials and metal-organic framework (MOF) materials hold significant promise for advanced energy systems. However, the accumulation of two-dimensional (2D) material and the low conductivity of MOF have seriously affected their practical application. The universal method for synthesizing homogeneous nitrogen-doped graphene-like carbon/metal-organic framework (N-GLC/MOF) composites, including N-GLC/MOF-74, N-GLC/ZIF-8, N-GLC/Cu-BTC, and N-GLC/FeCo-PBA was presented. Thanks to the synergistic effect of the two components, the N-GLC/MOF-74 composite exhibits a specific capacitance of 470.18 F/g at 1 A/g and maintains a coulombic efficiency of 95.04% at 5 A/g over 5500 cycles. Our work lays a solid foundation for the design and synthesis of N-GLC-based composites. We anticipate that this research will furnish valuable insights for the advancement of N-GLC/MOF composites, with a primary focus on enhancing supercapacitor performance.

Metal-organic frameworks (MOFs) are formed by the self-assembly of organic ligands with metal ions or clusters [1–3]. They go by the names of inorganic-organic hybrid materials, metal-organic coordination polymers, and porous coordination polymers [4]. MOFs are characterized by their large surface area, variable pore diameters, ultra-high porosity, and abundant redox-active metal centers [5–8]. As a result, MOFs have found extensive use in the fields of chemical sensing, gas storage, drug delivery, catalysis, and energy conversion [9,10]. Nevertheless, traditional MOFs exhibit suboptimal electrical conductivity, limiting their development in energy storage. Fortunately, the integration of MOFs with functional materials has emerged as a promising strategy that has greatly broadened the range of applications of MOFs [11]. Moreover, composites can retain the inherent advantages of a single component while exhibiting new physical and chemical properties that cannot be achieved with a single component.

Graphene-like materials, as versatile alternatives to graphene, have gained significant attention from researchers due to their unique characteristics [12]. They have an extremely high specific surface area, which allows supercapacitor to store more charge, thus improving the energy storage capacity [13]. Meanwhile, excellent electrical conductivity enables rapid transfer of charge, thereby increasing the power density of the supercapacitor [14]. More importantly, the structure and properties of graphene-like materials can be fine-tuned by adjusting the synthesis conditions and material compositions. By controlling the doping process, heteratom-doped graphene-like materials exhibit improved electrochemical properties, making them promising candidates for energy storage applications [15–17].

The combination of graphene-like materials with MOF in energy storage presents a synergistic approach aimed at enhancing electrochemical performance. This combination is driven by several factors and underscores its necessity for advancing energy storage technologies [18–20]. Firstly, the exceptional electrical conductivity of graphene-like materials provides a high-speed electron transport pathway within the composites. This, in turn, reduces internal resistance and allows for more efficient charge and discharge processes in energy storage devices [21]. Secondly, MOFs are renowned for their exceptional surface area and porosity, making them ideal candidates for supercapacitor electrodes. When combined with graphene-like materials, this high surface area is further optimized for improved ion adsorption and desorption. As a result, the energy storage capacity of supercapacitor is significantly increased, and rapid energy release becomes more feasible [22–24]. Additionally, MOFs' tunable chemical properties can be harnessed to design custom-tailored supercapacitor materials with enhanced energy storage and charge-discharge characteristics [25–27]. Thirdly, the structural flexibility of MOFs, when integrated with the mechanical strength of graphene-like materials, results in mechanically robust composites. This mechanical stability

---

[*] Corresponding author.
E-mail address: panghuan@yzu.edu.cn (H. Pang).

https://doi.org/10.1016/j.cclet.2024.109552

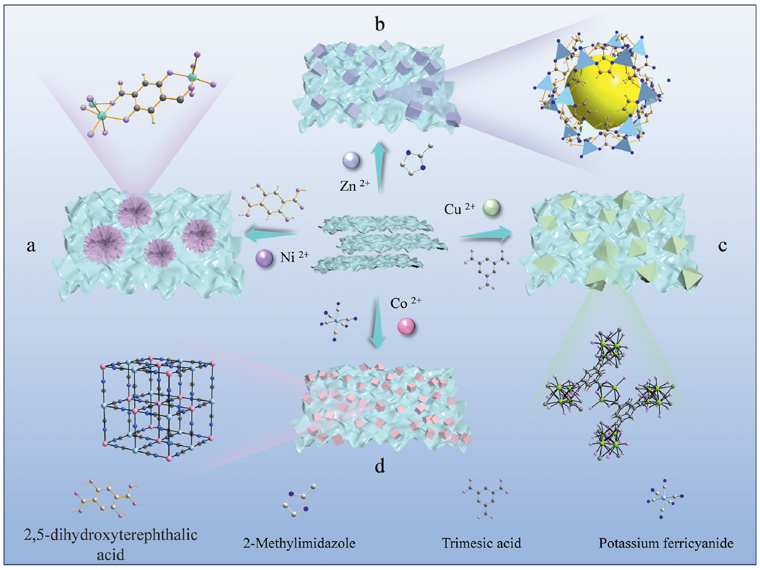

Fig. 1. Schematic of the synthesis of (a) N-GLC/MOF-74, (b) N-GLC/ZIF-8, (c) N-GLC/Cu-BTC, and (d) N-GLC/FeCo-PBA.

is crucial for the long-term performance of energy storage systems, as it mitigates the risk of structural degradation during charge-discharge cycles. Hence, the integration of graphene-like materials with MOFs in energy storage is essential to harness the synergistic benefits of enhanced electrical conductivity, improved gas adsorption, and mechanical stability [28,29]. These advantages collectively contribute to more efficient and durable energy storage systems, addressing the growing demand for advanced and sustainable energy technologies.

Herein, our work introduces a versatile synthesis method for composites, capitalizing on the straightforward production of nitrogen-doped graphene-like carbon (N-GLC). This method demonstrates broad applicability, particularly for materials with negatively charged surfaces. Thanks to the advantages of MOF and N-GLC, the properties of the composite have been greatly improved. Consequently, the N-GLC/MOF-74 electrode achieves a specific capacitance of 470.18 F/g at 1 A/g. Even after 5500 cycles at 5 A/g, the coulombic efficiency of N-GLC/MOF-74 remains 95.04%. Our study establishes a robust framework for designing and creating N-GLC-based composites, offering the adaptability to customize their structures for specific applications.

Typically, N-GLC is synthesized through the pyrolysis of a mixture of dicyandiamide and glucose in a nitrogen atmosphere. The introduction of dicyandiamide serves as a sacrificial template. During the initial heating stage, it leads to the formation of layered graphitic carbon nitride (g-C_3N_4), which subsequently combines with the aromatic carbon intermediates present in glucose. Eventually, under high-temperature conditions, these multilayered, corrugated N-GLC nanosheets are produced. The 2D morphology of N-GLC has been confirmed through scanning electron microscopy (SEM) (Fig. S1a in Supporting information) and transmission electron microscopy (TEM) (Fig. S1b in Supporting information). Additionally, selected area electron diffraction patterns indicate a relatively low degree of crystallinity throughout the carbon framework (Fig. S1c in Supporting information). Powder X-ray diffraction (XRD) analysis of the as-obtained samples further validates the structure, showing two broad peaks centered around 28° and 44°, which can be attributed to the (002) and (101) faces of graphitic carbon (Fig. S2 in Supporting information) [30]. The preparation procedures for N-GLC/MOF-74, N-GLC/ZIF-8, N-GLC/Cu-BTC, and N-GLC/FeCo-PBA composites are schematically presented in Fig. 1. The surface of N-GLC contains an abundance of functional groups, providing a negatively charged surface that facilitates the adsorption of metal cations. The surface termination groups of N-GLC subsequently form a cross-link with these metal ions, which effectively reduces the electrostatic repulsion between the nanosheets and acts as a nucleation site for the *in-situ* growth of MOF. As a result, MOF-74, ZIF-8, Cu-BTC, and FeCo-PBA can grow *in-situ* on the N-GLC through a coprecipitation reaction (Figs. 1a–d).

The SEM images (Figs. 2a, e, i, and m) indicate that the N-GLC/MOF composites consist of N-GLC and MOF particles. This observation is corroborated by the TEM images (Figs. 2b, c, f, g, j, k, n, and o). To compare the material properties, we also prepared rGO-related and g-C_3N_4-related composites. The SEM images of rGO/MOF-74 and g-C_3N_4/MOF-74 are presented in Fig. S3 (Supporting information). The successful synthesis of rGO-related and g-C_3N_4-related composites serves as evidence that this synthesis method possesses universality. Further, high-angle annular dark-field scanning transmission electron microscopy (HAADF-STEM) and corresponding elemental mapping images (Figs. 2d, h, l, and p) proved the uniform distribution of elements on the N-GLC/MOF composites. This reaffirms that MOF particles are intimately and uniformly integrated with the N-GLC substrate. In Raman spectra, the observed intensity ratios of the D and G bands are indicative of the defect levels in the material. Specifically, a ratio of around 1.01 is found for the N-GLC substrates. For the N-GLC/MOF-74 composite, this ratio is slightly lowered, registering at about 0.94, as shown in Fig. S4 (Supporting information). Meanwhile, the N-GLC/ZIF-8, N-GLC/Cu-BTC, and N-GLC/FeCo-PBA composites demonstrate D to G peak intensity ratios of 0.99, 0.96, and 1.00, respectively (Fig. S5 in Supporting information) [31]. These defects often serve as active sites or anchoring points, facilitating the uniform attachment and dispersion of metal atoms. The XRD patterns offer additional evidence to the composites formation and the interactions to these components. Evidently, peaks attributed to MOF-74 and N-GLC can be found in the N-GLC/MOF-74 composite (Fig. 3a) [32]. The same results were observed in N-GLC/ZIF-8, N-GLC/Cu-BTC, and N-GLC/FeCo-PBA composites (Figs. S6–S8 in Supporting information). This simultaneous observation of peaks indicates the harmonious integration of both materials, indicating the successful preparation of the composites.

Fourier-transform infrared (FT-IR) spectra were acquired to determine the molecular structure and chemical composition of the

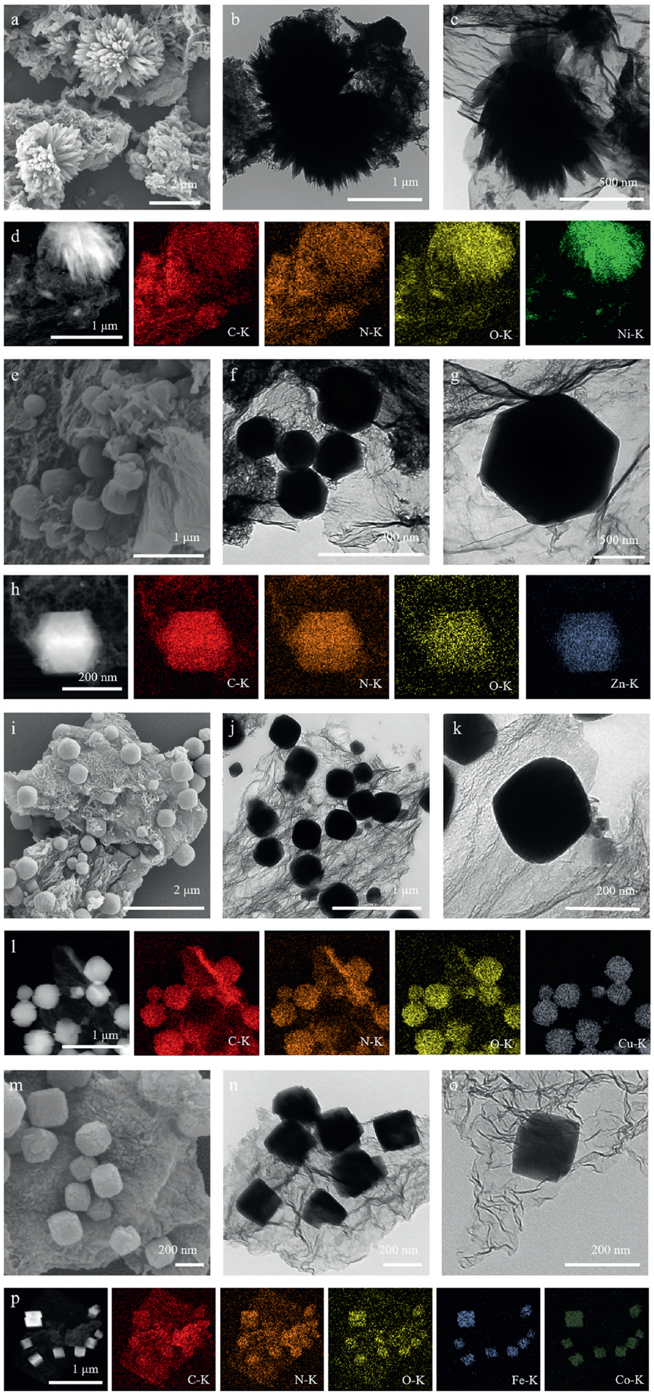

Fig. 2. (a, e, i, m) SEM, (b, c, f, g, j, k, n, o) TEM, (d, h, l, p) HAADF-STEM images and element mapping of (a–d) N-GLC/MOF-74. (e–h) N-GLC/ZIF-8, (i–l) N-GLC/Cu-BTC, and (m–p) N-GLC/FeCo-PBA.

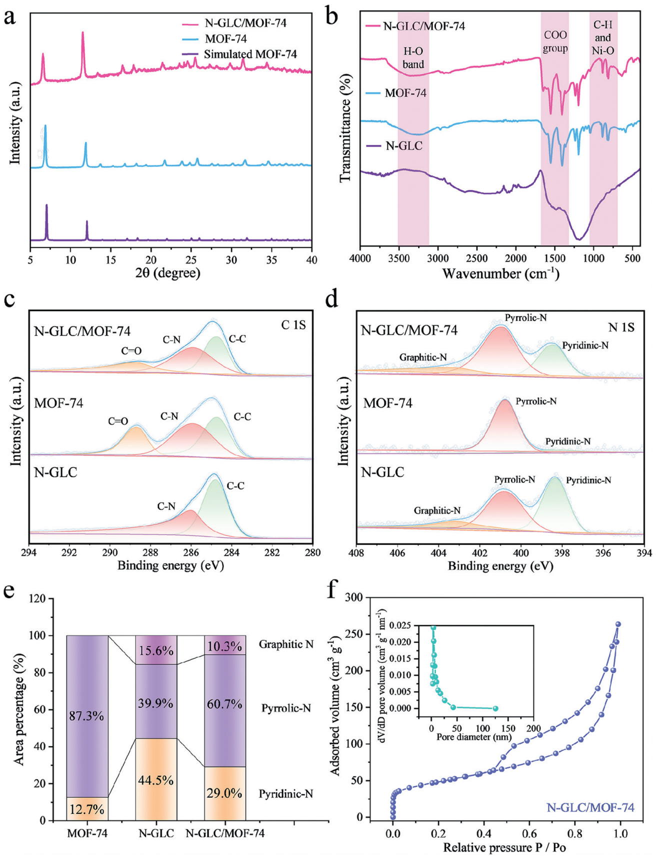

Fig. 3. (a) XRD of MOF-74, N-GLC/MOF-74. (b) FT-IR of N-GLC, MOF-74, and N-GLC/MOF-74. (c) C 1s XPS spectra of N-GLC, MOF-74, and N-GLC/MOF-74. (d) N 1s XPS spectra of N-GLC, MOF-74, and N-GLC/MOF-74. (e) The percentage of pyridinic-N, pyrrolic-N, and graphitic-N for N-GLC, MOF-74, and N-GLC/MOF-74. (f) N2 adsorption-desorption isotherms and pore size distributions of N-GLC/MOF-74.

sample. For N-GLC/MOF-74, we observed the characteristic peaks at approximately 1550 and 1404 $\mathrm{cm^{-1}}$, which can be attributed to the stretching vibrations of symmetric and asymmetric carboxylic acid groups (COO-) (Fig. 3b). Additionally, peaks at 887, 812, and 3390 $\mathrm{cm^{-1}}$ are associated with the stretching vibrations of the Ni-O, C-H, and -OH bonds, respectively. For N-GLC/ZIF-8 (Fig. S9 in Supporting information) [33], the peak at 993 $\mathrm{cm^{-1}}$ is attributed to the vibration of the C-N bond. The stretching vibrations of the C-H bond (3131 and 2919 $\mathrm{cm^{-1}}$) in the methyl group and the imidazole ring were also evident in the spectrum. The FT-IR spectrum of N-GLC/Cu-BTC is presented in Fig. S10 (Supporting information) [34]. The characteristic peaks at 1644 and 1589 $\mathrm{cm^{-1}}$ correspond to the symmetric tensile vibration of the H_3BTC skeleton, while the characteristic peaks at 1446 and 1373 $\mathrm{cm^{-1}}$ correspond to the antisymmetric tensile vibration of the H_3BTC skeleton. Furthermore, bands between 1108 and 1290 $\mathrm{cm^{-1}}$ can be attributed to the stretching vibration of the C=O bond, and the bending vibration of the C-H bonds are observed at 939 to 580 $\mathrm{cm^{-1}}$. The peaks at 728 and 489 $\mathrm{cm^{-1}}$ correspond to the stretching and bending vibrations of the Cu-O coordination. For N-GLC/FeCo-PBA (Fig. S11 in Supporting information) [35], the prominent peak is located at 2115 $\mathrm{cm^{-1}}$, characteristic of the C≡N stretching. The peak at 592 $\mathrm{cm^{-1}}$ is attributed to the Fe-CN vibration, while the peak at 547 $\mathrm{cm^{-1}}$ corresponds to the stretching mode of Fe-O. Additionally, the wide absorption peaks observed at 1600 and 3621 $\mathrm{cm^{-1}}$ are associated with O-H stretching and H-O-H bending modes. The positions of the absorption peaks observed in the N-GLC/FeCo-PBA sample closely match those of the FeCo-PBA, indicating the presence of the prussian blue structure in the N-GLC/FeCo-PBA composite. The above results suggest that the N-GLC matrix effectively incorporates the MOF clusters, maintaining their characteristic properties.

X-ray photoelectron spectroscopy (XPS) was used to analyze the molecular composition and valence state of N-GLC, MOF-74, and N-GLC/MOF-74. The survey spectra (Fig. S12 in Supporting information) indicate the presence of C, N, O, and Ni in the samples. For N-GLC, only C-C (284.80 eV) and C-N (285.9 eV) bonds are present. However, the C=O (289.06 eV) bond is found in N-GLC/MOF-74, attributed to MOF-74 (Fig. 3c) [36]. Two peaks (398.3 eV and 400.8 eV), corresponding to pyridinic-N and pyrrolic-N, are visible

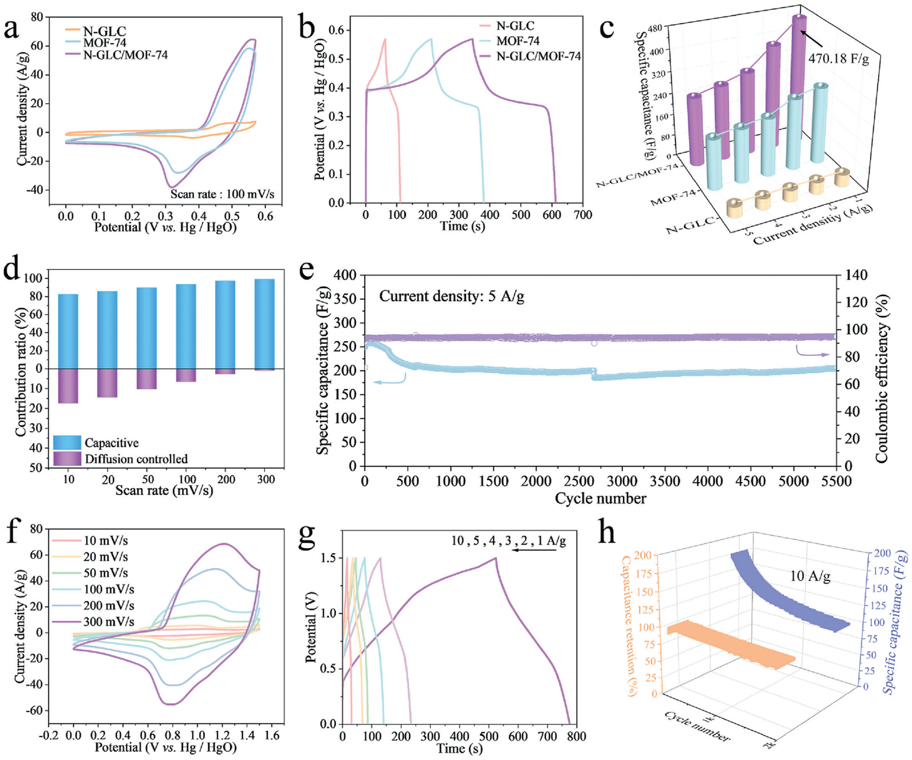

Fig. 4. (a) CV curves of N-GLC, MOF-74, and N-GLC/MOF-74 at 100 mV/s. (b) GCD curves of N-GLC, MOF-74, and N-GLC/MOF-74 at 1 A/g. (c) Specific capacitance of N-GLC, MOF-74, and N-GLC/MOF-74 at current densities from 1 A/g to 5 A/g. (d) Capacitive contributions of N-GLC/MOF-74. (e) Long-term cycling stability of N-GLC/MOF-74 over 5500 GCD cycles at a current density of 5 A/g. (f) CV curves of N-GLC/MOF-74//AC at different scanning rates. (g) GCD curves of N-GLC/MOF-74//AC at different current density. (h) The cycling stability and capacitance retention at 10 A/g for 1869 cycles of N-GLC/MOF-74//AC.

in the N 1s XPS spectra of N-GLC, MOF-74, and N-GLC/MOF-74 (Fig. 3d). Meanwhile, the graphitic N (403.2 eV) belonging to N-GLC is observed in N-GLC/MOF-74 composite. These all confirm the synthesis of N-GLC/MOF-74 composite. Further, quantitative analysis can be performed by integrating the areas under each species-specific peak in the N 1s XPS spectra. The relative abundance of pyridinic-N in the N-GLC/MOF-74 increased sharply from 12.7% (MOF-74) to 29.0% (Fig. 3e). Interestingly, pyridinic-N is believed to contribute to pseudocapacitance through protonation, while simultaneously participating in the modulation of the electronic structure and providing coordination sites [37,38]. It is foreseeable that the N-GLC/MOF-74 composite will exhibit excellent capacitive properties. In Fig. S13 (Supporting information), the Ni 2p XPS are depicted, from which four peak positions were obtained [39]. The peaks at 855.9 eV and 873.6 eV correspond to Ni $2p_{3/2}$ and Ni $2p_{1/2}$, respectively, signifying the presence of Ni^{2+}. Meanwhile, the peaks at 860.9 eV and 878.4 eV are associated with satellite peaks.

The specific surface areas and pore size distribution was measured by Branauer–Emmett–Teller (BET) and Barret–Joyner–Halenda (BJH) methods. For N-GLC, a specific surface area of 439.662 m^2/g and a pore size of 3.63 nm were obtained (Fig. S14 in Supporting information). MOF-74 shows a specific surface area of 52.626 m^2/g and a pore size of 2.07 nm (Fig. S15 in Supporting information). Notably, the N-GLC/MOF-74 composite demonstrates a significant enhancement in surface area, reaching 156.384 m^2/g with a pore size of 4.21 nm (Fig. 3f). According to the IUPAC standard, the nitrogen adsorption isotherms of the three materials showed type IV characteristics [40].

All the samples were tested by cyclic voltammetry (CV) and galvanostatic charge–discharge (GCD) tests under the same conditions. The area surrounded by CV reflects the capacitance of the material, so it can be expected that N-GLC/MOF-74 has a larger specific capacitance than that of N-GLC and MOF-74 (Fig. 4a). Additionally, obvious REDOX peaks appear in the CV curves of MOF-74, N-GLC, and N-GLC/MOF-74, indicating their Faraday pseudocapacitance characteristics (Figs. S16–S18 in Supporting information). The same conclusion was obtained by comparing the GCD curves of N-GLC, MOF-74, and N-GLC/MOF-74 electrodes at 1 A/g (Fig. 4b). According to the specific capacitance calculation formula, the specific capacitance of the N-GLC/MOF-74 electrode was 470.18 F/g, which was higher than those of MOF-74 (295.26 F/g) and N-GLC (18.95 F/g) electrodes at 1 A/g (Fig. 4c). Moreover, we have made a comprehensive comparison with relevant works in this field (Table S1 in Supporting information). In addition, the N-GLC/MOF-74 was tested under higher current density (10, 20, 30, 40, and 50 A/g), and the relevant GCD curves and specific capacitance were demonstrated in Figs. S19 and S20 (Supporting information).

To further illustrate the superiority of the N-GLC/MOF-74 electrode, we conducted a comparative analysis of its performance against rGO/MOF-74 and g-C_3N_4/MOF-74. By comparing CV curves at 100 mV/s, it can be seen that N-GLC/MOF-74 has the largest enclosed area (Fig. S21 in Supporting information). The GCD curves of the N-GLC/MOF-74, rGO/MOF-74 and g-C_3N_4/MOF-74 electrodes at 1 A/g are depicted in Fig. S22 (Supporting information). Further insights into the specific capacitances of rGO/MOF-74 and g-C_3N_4/MOF-74 in the range of 1–5 A/g are provided in Figs. S23 and S24 (Supporting information). Notably, the results demonstrate that N-GLC/MOF-74 exhibits a higher specific capacitance compared to the other materials. This can be attributed to N-GLC providing superior electrical conductivity, facilitating rapid electron transfer within the electrode. This not only reduces internal resistance but also allows for more efficient charge and discharge processes, ultimately contributing to the superior specific capacitance. The compelling advantages of N-GLC/MOF-74 underline its potential as a high-performance electrode material, making it a viable option for a variety of energy storage uses.

It is interesting to note that when the scan rate increased from 10 mV/s to 300 mV/s (Fig. S25 in Supporting information), the capacitive contributions of N-GLC/MOF-74 showed progressive rising trends from 82.6% to 99.1%, highlighting the critical role of capacitive storage (Fig. 4d). Furthermore, the Nyquist plots indicate that the electron transfer of the composites is significantly enhanced (Fig. S26 in Supporting information). It is remarkable that at 5 A/g, the N-GLC/MOF-74 electrode maintained a high specific capacitance of 204.73 F/g. After 5500 GCD cycles at 5 A/g, N-GLC/MOF-74 achieves a coulombic efficiency of 95.04% (Fig. 4e). This indicates that the electrode maintains its high performance even after extended cycling, highlighting its suitability for long-term energy storage applications. The morphology, structure (Fig. S27 in Supporting information) and composition (Fig. S28 in Supporting information) of the N-GLC/MOF-74 after cycling was also examined.

The asymmetric two-electrode system was constructed based on the N-GLC/MOF-74 electrodes, denoted as N-GLC/MOF-74//AC (activated carbon). The obvious redox character and exceptional rate performance of N-GLC/MOF-74//AC are demonstrated by the CV curves, which at various scan rates all maintained their original forms (Fig. 4f). The GCD curve of N-GLC/MOF-74//AC is symmetrical (Fig. 4g), indicating that N-GLC/MOF-74//AC has excellent fast charge-discharge characteristics. Furthermore, at a high current density of 10 A/g, the capacitance retention for N-GLC/MOF-74//AC is close to 90% (Fig. 4h). The energy densities reached 52.5 µWh/cm^2 at 0.75 mW/cm^2 and remained at 33.75 µWh/cm^2 at 3.75 mW/cm^2 (Fig. S29 in Supporting information). The outstanding electrochemical performance can be attributed to the following two points: First, the introduction of 3D MOF avoids serious agglomeration of 2D materials. Second, as a superior conductor, the N-GLC makes it easier for electrons to flow during charge and discharge.

In summary, our study proposes a general composites synthesis method based on the direct synthesis of N-GLC. This method is suitable for materials of different dimensions, especially those with negatively charged surfaces. The N-GLC/MOF-74 electrode, synthesized using this method, exhibits a favorable specific capacity of 470.18 F/g at a current density of 1 A/g. Furthermore, the coulombic efficiency of N-GLC/MOF-74 remains 95.04% after 5500 cycles at 5 A/g. Our work lays a robust foundation for the design and synthesis of N-GLC-based composites, offering the flexibility to tailor their structures to specific applications. We anticipate that our work will offer valuable insights for the development of N-GLC/MOF composites, with the ultimate goal of enhancing supercapacitor performance.

Declaration of competing interest

The authors declare that they have no known competing financial interests or personal relationships that could have appeared to influence the work reported in this paper.

Acknowledgments

This work was supported by National Natural Science Foundation of China (No. U1904215), Natural Science Foundation of Jiangsu Province (No. BK20200044) and Changjiang scholars program of the Ministry of Education (No. Q2018270). We also acknowledge the Priority Academic Program Development of Jiangsu Higher Education Institutions and the technical support we received at the Testing Center of Yangzhou University.

Supplementary materials

Supplementary material associated with this article can be found, in the online version, at doi:10.1016/j.cclet.2024.109552.

References

[1] T. Lv, G. Zhu, S. Dong, et al., Angew. Chem. Int. Ed. 62 (2023) e202216089.
[2] Y. Peng, Y. Bai, C. Liu, et al., Coord. Chem. Rev. 466 (2022) 214602.
[3] P. Geng, L. Wang, M. Du, et al., Adv. Mater. 34 (2022) 2107836.
[4] X. Wang, H. Hong, S. Yang, et al., Inorg. Chem. Front. 10 (2023) 2115.
[5] J. Zhao, Y. Jiang, H. Fan, et al., Adv. Mater. 29 (2017) 1604569.
[6] Y. Song, X. Song, X. Wang, et al., J. Am. Chem. Soc. 144 (2022) 17457.
[7] W.H. Li, K. Ding, H.R. Tian, et al., Adv. Funct. Mater. 27 (2017) 1702067.
[8] Z. Xiao, Y. Mei, S. Yuan, et al., ACS Nano 13 (2019) 7024.
[9] L. Wang, X. Feng, L. Ren, et al., J. Am. Chem. Soc. 137 (2015) 4920.
[10] T. Deng, Y. Lu, W. Zhang, et al., Adv. Energy Mater. 8 (2018) 1702294.
[11] S. Zhou, X. Kong, B. Zheng, et al., ACS Nano 13 (2019) 9578.
[12] X.-H. Li, S. Kurasch, U. Kaiser, M. Antonietti, Angew. Chem. Int. Ed. 51 (2012) 9689.
[13] Y. Li, Z. Li, P.K. Shen, Adv. Mater. 25 (2013) 2474.
[14] Y. Li, Z.S. Wu, P. Lu, et al., Adv. Sci. 7 (2020) 1903089.
[15] Y. Deng, T. Shang, Z. Wu, et al., Adv. Mater. 31 (2019) 1902432.
[16] S. Selvam, Y.K. Park, J.H. Yim, Adv. Sci. 9 (2022) 2201890.
[17] Y. Xu, Y. Tao, X. Zheng, et al., Adv. Mater. 27 (2015) 8082.
[18] H. Zhu, Q. Jiao, R. Fu, et al., J. Colloid Interface Sci. 613 (2022) 182.
[19] Y. Li, Y. Xu, W. Yang, et al., Small 14 (2018) 1704435.
[20] J. Aguilera-Sigalat, D. Bradshaw, Coord. Chem. Rev. 307 (2016) 267.
[21] Y. Peng, J. Xu, J. Xu, et al., Adv. Colloid Interface Sci. 307 (2022) 102732.
[22] G. Duan, H. Zhang, C. Zhang, S. Jiang, H. Hou, Chin. Chem. Lett. 34 (2023) 108283.
[23] Y. Chen, J. Lei, Y. Zhai, et al., Chin. Chem. Lett. 34 (2023) 108305.
[24] G. Yang, C. Pei, F. Xu, et al., Chin. Chem. Lett. 34 (2023) 108152.
[25] H. Chen, X.F. Liu, H.Y. Li, P. Peng, S.Q. Zang, Nano Res. 15 (2022) 6208.
[26] O. Basu, S. Mukhopadhyay, S. Laha, S.K. Das, Chem. Mater. 34 (2022) 6734.
[27] M.A. Tahir, N. Arshad, M. Akram, J. Energy Storage 47 (2022) 103530.
[28] J. Gu, H. Fan, C. Li, J. Caro, H. Meng, Angew. Chem. Int. Ed. 58 (2019) 5297.
[29] D.S. Raja, X.F. Chuah, S.Y. Lu, Adv. Energy Mater. 8 (2018) 1801065.
[30] D. Yao, C. Tang, X. Zhi, et al., Adv. Mater. 35 (2023) 2209386.
[31] N. Li, L. Li, J. Xia, et al., J. Mater. Sci. Technol. 139 (2023) 224.
[32] T. Li, Z. Jin, J. Colloid Interface Sci. 605 (2022) 385.
[33] H. Zhang, M. Zhao, Y. Yang, Y.S. Lin, Microporous Mesoporous Mater. 288 (2019) 109568.
[34] R. Pan, Y. Guo, Y. Tang, et al., Chem. Eng. J. 430 (2022) 132127.
[35] R. Zhou, P. Wang, Y. Guo, et al., Nanoscale 11 (2019) 19497.
[36] J. Lim, S. Lee, H. Ha, et al., Angew. Chem. Int. Ed. 60 (2021) 9296.
[37] Z. Wang, B. Jin, J. Peng, et al., Adv. Funct. Mater. 31 (2021) 2102300.
[38] J. Xu, F. Xu, M. Qian, F. Xu, Z. Hong, F. Huang, Adv. Mater. 29 (2017) 1701674.
[39] T. Chen, F. Wang, S. Cao, et al., Adv. Mater. 34 (2022) 2201779.
[40] Y. Zhang, G. Wang, W. Ma, B. Ma, Z. Jin, Dalt. Trans. 47 (2018) 11176.